g factor of chiral doublets with $\pi(1h_{11/2})^1 \otimes \nu(1h_{11/2})^{-1}$ configuration

Q. B. Chen [*]

Department of Physics, East China Normal University, Shanghai 200241, China

(Received 30 August 2023; accepted 5 January 2024; published 8 February 2024)

The g factor of chiral doublet bands has been extensively studied within the framework of the particle rotor model. Specifically, these investigations have focused on systems characterized by the particle-hole configuration $\pi(1h_{11/2})^1 \otimes \nu(1h_{11/2})^{-1}$. Comprehensive examinations have been carried out to assess the influence of deformation parameters β and γ, the moment of inertia $\mathcal{J}_0$, the total spin I, and the angular momentum of the collective rotor j_R on the g factor. The findings reveal that the g factor exhibits insensitivity to variations in $\mathcal{J}_0$ and β values, while its behavior is highly sensitive to changes in the γ parameter. Moreover, it has been observed that the g factors and the $g(j_R)$ plots associated with the doublet bands demonstrate remarkable similarity in the static chirality region. However, noticeable differences arise in regions characterized by chiral vibration or lacking chirality.

DOI: 10.1103/PhysRevC.109.024308

I. INTRODUCTION

The phenomenon of nuclear chirality can manifest in rapidly rotating nuclei characterized by a triaxially deformed core and populated by high-j valence particles and holes [1]. In the body-fixed frame, the angular momenta of the valence particles and holes align along the principal axes of the triaxial core, with the short axis aligningwith their angular momenta and the long axis aligned with the holes. Simultaneously, the rotational core aligns its angular momentum along the intermediate axis. Consequently, the left-handed and right-handed orientations of these three angular momenta become degenerate, potentially leading to a spontaneous breaking of chiral symmetry. However, in the laboratory frame, the requirements of time-reversal invariance and quantum-mechanical tunneling allow for the restoration of chiral symmetry by facilitating the exchange of total angular momentum between the left-handed and right-handed configurations. As a result, the expected observation involves chiral doublet bands, characterized by nearly degenerate $\Delta I = 1$ bands sharing the same parity [1].

To date, the observation of more than 50 candidate nuclei exhibiting chirality has been documented in mass regions around $A \approx 80$, 100, 130, and 190. The extensive research conducted in this field can be explored further through recent reviews such as Refs. [2–9], along with the corresponding data tables provided in Ref. [10]. Notably, the predictions [11–17] and confirmations [18–26] of multiple chiral doublet bands within a single nucleus have significantly advanced the investigation of chirality in nuclear structure physics, sustaining the ongoing interest and significance of this research area.

In addition to energy spectra, electromagnetic transition strengths serve as important observables for the identification of nuclear chirality. In a model utilizing the configuration $\pi(1h_{11/2}) \otimes \nu(1h_{11/2})^{-1}$ and a triaxial deformation parameter of $\gamma = 30^\circ$, ideal nuclear chirality is determined based on certain criteria outlined in references such as Refs. [1,2,5,27–38]. Specifically, these criteria specify that there should be similarities in the reduced magnetic dipole ($M1$) and electric quadrupole ($E2$) transition strengths within a band (intraband) as well as between different bands (interband). Such observations play a crucial role in the analysis and determination of nuclear chirality.

The exploration of additional observables that serve to characterize nuclear chirality remains a compelling research question. Very recently, we have embarked on the novel investigation of the static (electric) quadrupole moment (SQM), also known as the spectroscopic quadrupole moment, pertaining to nuclear chiral doublet bands [39]. This examination marks the first exploration of SQMs in the context of chiral nuclear systems. The SQM is intricately linked to both intrinsic deformation parameter (a static property) and the orientation of the total angular momentum (a dynamic property) of the nuclear system. The SQM serves as a fundamental indicator of the charge distribution associated with rotational motion, thereby aiding in the discernment of whether the angular momenta have given rise to configurations associated with chiral vibration or static chirality. Through the study of SQMs, one gleans essential insights into the nature and characteristics of these intriguing phenomena in nuclear structure. It is worth mentioning here that the SQM has also been used to investigate the angular momentum coupling scheme in wobbling motion in Refs. [40,41].

Furthermore, a significant breakthrough has been achieved with the first-ever measurement of the g factor (gyromagnetic ratio) in a chiral band, specifically for the bandhead of ^{128}Cs [42,43]. The determination of the g factor provides vital information concerning the relative orientation of the three angular momentum vectors associated with the particle, the

[*]qbchen@phy.ecnu.edu.cn

hole, and the nuclear core. It enables the distinction between whether these three angular momentum vectors lie within a plane (referred to as a planar configuration or chiral vibration) or span across three-dimensional space (known as an aplanar configuration or static chirality). This pioneering measurement of the g factor offers novel insights and prospects for further understanding the intricate nature of nuclear chirality. Note that the configuration of the bands in ^{128}Cs is $\pi(1h_{11/2})^1 \otimes \nu(1h_{11/2})^{-5}$ [42,43]. In the context of the neutron component, the notation -5 signifies the presence of five unoccupied states, or "holes," within the $h_{11/2}$ shell. Further, four of these holes are paired in such a way that they occupy the time and time-reversed states. Based on this configuration, Ref. [42] focused on the study of the g factor for the bandhead ($I = 9\hbar$) of ^{128}Cs and Ref. [42] focused further on the g factor of the yrast band ($9\hbar \leqslant I \leqslant 20\hbar$) in ^{128}Cs.

In this work, my focus centers on investigating the g factors for not only the yrast band but also the yrare band within a simplified configuration, namely, $\pi(1h_{11/2})^1 \otimes \nu(1h_{11/2})^{-1}$. By examining this specific configuration, I aim to unravel the intricate interplay between the valence proton, the valence neutron, and the core constituents and their respective contributions to the g factor. Additionally, this simplified configuration allows for a more focused exploration of the underlying nuclear structure and its manifestation in the magnetic properties of the system.

My calculations in this study are based on the widely utilized particle rotor model (PRM), which has demonstrated significant success in describing chiral doublet bands, as evidenced by previous works [1,7,27,36,38,44–49]. This quantum-mechanical model integrates the collective rotational motion with intrinsic single-particle motions, providing a comprehensive description of the nuclear system within the laboratory frame. The Hamiltonian of the PRM is diagonalized considering states with the total angular momentum as a fundamental quantum number. Through the diagonalization process, one can directly obtain the energy splitting and quantum-mechanical tunneling probabilities between the doublet bands. Importantly, the underlying inputs required by the PRM are derived from the covariant density functional theory [11,50], and for practical applications, please refer to related references [18–20,23,34,42,48,51–53]. Consequently, the PRM affords a straightforward approach to investigate the g factor of chiral doublet bands with the given framework and methodology.

II. THEORETICAL FRAMEWORK

A. Particle rotor model

In the PRM, the Hamiltonian describing a system consisting of one proton and one neutron coupled to a triaxial rigid rotor can be formulated as follows [1,7,27,36,38,44–49]:

$$\hat{H}_{\rm PRM} = \hat{H}_{\rm coll} + \hat{H}_p + \hat{H}_n, \tag{1}$$

where $\hat{H}_{\rm coll}$ represents the Hamiltonian of the rigid rotor,

$$\hat{H}_{\rm coll} = \sum_{k=1}^{3} \frac{\hat{j}_{Rk}^2}{2\mathcal{J}_k} = \sum_{k=1}^{3} \frac{(\hat{I}_k - \hat{j}_{pk} - \hat{j}_{nk})^2}{2\mathcal{J}_k}. \tag{2}$$

In this formula, the index $k = 1$, 2, and 3 corresponds to components aligned with the three principal axes within the body-fixed frame. The Hamiltonian incorporates various operators: $\hat{j}_{Rk}$ and $\hat{I}_k$ signify the angular momentum operators of the collective rotor and the total nucleus, respectively, while $\hat{j}_{p(n)k}$ represents the angular momentum operator of the valence proton (neutron). The parameters $\mathcal{J}_k$ correspond to the three principal moments of inertia characterizing the system.

The Hamiltonians $\hat{H}_p$ and $\hat{H}_n$ are employed to describe the behavior of a single proton and neutron, respectively, situated outside the collective rotor. For a nucleon in a j-shell orbital, $\hat{H}_{p(n)}$ is given by

$$\hat{H}_{p(n)} = \pm\frac{C}{2}\left\{\cos\gamma\left[\hat{j}_3^2 - \frac{j(j+1)}{3}\right] + \frac{\sin\gamma}{2\sqrt{3}}(\hat{j}_+^2 + \hat{j}_-^2)\right\}, \tag{3}$$

where the sign $\pm$ refers to a particle or hole and γ is the triaxial deformation parameter. The coupling parameter C exhibits a proportionality relationship with the quadrupole deformation parameter β associated with the collective rotor. This implies that changes in β directly influence the magnitude of C, establishing a connection between the structural deformations of the rotor and the strength of the coupling within the system.

B. Weak-coupling basis

The PRM Hamiltonian presented in Eq. (1) can be effectively solved through diagonalization within the framework of the weak-coupling basis [38], which is a product of the states of proton $|j_p\rangle$, neutron $|j_n\rangle$, and core $|j_R\rangle$, respectively. The three angular momenta are coupled to the total angular momentum as follows: $\boldsymbol{j}_p$ and $\boldsymbol{j}_n$ are coupled to a vector $\boldsymbol{j}_{pn} = \boldsymbol{j}_p + \boldsymbol{j}_n$ which, in turn, is coupled with $\boldsymbol{j}_R$ to $\boldsymbol{I} = \boldsymbol{j}_{pn} + \boldsymbol{j}_R$. In detail,

$$\begin{aligned}&|(j_p j_n) j_{pn} j_R; IM\rangle \\ &= \sum_{m_p,m_n,m_{pn},m_R} \langle j_p m_p j_n m_n | j_{pn} m_{pn}\rangle \\ &\quad \times \langle j_{pn} m_{pn} j_R m_R | IM\rangle |j_p m_p\rangle |j_n m_n\rangle |j_R m_R\rangle,\end{aligned} \tag{4}$$

where first the coupling of $\boldsymbol{j}_p$ and $\boldsymbol{j}_n$ to $\boldsymbol{j}_{pn}$ is performed and after that $\boldsymbol{j}_{pn}$ and the rotor quantum number $\boldsymbol{j}_R$ are coupled to the total angular momentum $\boldsymbol{I}$. In the above expression, m_R, m_{pn}, and $m_{p(n)}$ are the projection quantum numbers of $\boldsymbol{j}_R$, $\boldsymbol{j}_{pn}$, and $\boldsymbol{j}_{p(n)}$ on the z axis in the laboratory frame, respectively. Obviously, the appearance of Clebsch-Gordan coefficients requires $M = m_{pn} + m_R = m_p + m_n + m_R$. The value of j_{pn} is in the range $|j_p - j_n| \leqslant j_{pn} \leqslant j_p + j_n$. Accordingly, for a given j_{pn}, the value of j_R must satisfy the triangular condition $|I - j_{pn}| \leqslant j_R \leqslant I + j_{pn}$ of the angular momentum coupling. There are several possible j_{pn} quantum numbers, indicating that the total spin state $|IM\rangle$ may be formed in several ways, here called coupling schemes. A single coupling scheme given by Eq. (4) defines a unique set of expected mutual angles between each pair of the angular momentum vectors.

In general, the state with definite spin $|IM\rangle$ is a superposition of many coupling schemes (only the angular momentum

quantum numbers are exposed):

$$|IM\rangle = \sum_{j_p, j_n, j_{pn}, j_R} c_{I j_p j_n j_{pn} j_R} |(j_p j_n) j_{pn} j_R; IM\rangle, \tag{5}$$

with the superposition coefficients $c_I(j_p, j_n, j_{pn}, j_R)$ obtained by diagonalizing the Hamiltonian $\hat{H}_{\rm PRM}$ (1).

C. g factor

The g factor of the studied system is defined in terms of the magnetic moment. This factor captures the ratio between the magnetic moment and the angular momentum of the system, shedding light on the intrinsic magnetic properties and the behavior of the nuclear system under external magnetic fields. By investigating and analyzing the g factor, one can gain valuable insights into the underlying spin dynamics and the coupling between the angular momentum and the magnetic moment within the system. The magnetic moment is defined as the expectation value of the z component of the magnetic moment operator $\hat{\boldsymbol{\mu}}$ in the state $|II\rangle$ in which the z component of the angular momentum M takes its maximal value as $M = I$,

$$\begin{aligned}\mu(I) &= g(I) I = \langle II | g I_z | II \rangle \\ &= \langle II | g_p j_{pz} + g_n j_{nz} + g_R j_{Rz} | II \rangle \\ &= \frac{\langle II | g_p \boldsymbol{j}_p \cdot \boldsymbol{I} + g_n \boldsymbol{j}_n \cdot \boldsymbol{I} + g_R \boldsymbol{j}_R \cdot \boldsymbol{I} | II \rangle}{I(I+1)} \langle II | I_z | II \rangle. \end{aligned} \tag{6}$$

In the above derivation, I have used the projection theorem, also known as the Landé formula. Further using the following relations

$$\boldsymbol{I} = \boldsymbol{j}_p + \boldsymbol{j}_n + \boldsymbol{j}_R, \tag{7}$$

$$\langle \boldsymbol{I}^2 \rangle = I(I+1), \tag{8}$$

$$\langle \boldsymbol{j}^2_{p(n)} \rangle = j_{p(n)}(j_{p(n)}+1), \tag{9}$$

one gets

$$\begin{aligned} g(I) &= \frac{1}{\langle \boldsymbol{I}^2 \rangle} \langle g_p \boldsymbol{j}_p \cdot \boldsymbol{I} + g_n \boldsymbol{j}_n \cdot \boldsymbol{I} + g_R \boldsymbol{j}_R \cdot \boldsymbol{I} \rangle \\ &= g_R + \frac{1}{\langle \boldsymbol{I}^2 \rangle} \langle (g_p - g_R) \boldsymbol{j}_p \cdot \boldsymbol{I} + (g_n - g_R) \boldsymbol{j}_n \cdot \boldsymbol{I} \rangle \\ &= g_R + g^{(p)} + g^{(n)} \\ &= g_{\rm chiral} - \frac{1}{\langle \boldsymbol{I}^2 \rangle} (g_p \langle \boldsymbol{j}_n \cdot \boldsymbol{j}_R \rangle + g_n \langle \boldsymbol{j}_p \cdot \boldsymbol{j}_R \rangle + g_R \langle \boldsymbol{j}_p \cdot \boldsymbol{j}_n \rangle). \end{aligned} \tag{10}$$

In the aforementioned analysis, I incorporate the individual contributions to the g factors originating from the proton and neutron constituents:

$$g^{(p)} = (g_p - g_R) \sqrt{\frac{j_p(j_p+1)}{I(I+1)}} \cos\theta_{pI}, \tag{11}$$

$$g^{(n)} = (g_n - g_R) \sqrt{\frac{j_n(j_n+1)}{I(I+1)}} \cos\theta_{nI}, \tag{12}$$

which are determined by the effective angles between the proton (neutron) and the total angular momenta θ_{pI} (θ_{nI}). By considering these distinct components, I aim to provide a comprehensive understanding of the overall g-factor behavior within the system, taking into account the specific effects and interactions of both valence protons and valence neutrons.

In addition, I introduce the g factor in the limit of the ideal chiral geometry with the proton, neutron, and rotor angular momentum vectors being mutually perpendicular $\boldsymbol{j}_p \perp \boldsymbol{j}_n \perp \boldsymbol{j}_R$,

$$\begin{aligned} g_{\rm chiral} = \frac{1}{2} \Bigg[&(g_p + g_n + g_R) + (g_p - g_n - g_R) \frac{\langle \boldsymbol{j}^2_p \rangle}{\langle \boldsymbol{I}^2 \rangle} \\ &+ (g_n - g_p - g_R) \frac{\langle \boldsymbol{j}^2_n \rangle}{\langle \boldsymbol{I}^2 \rangle} + (g_R - g_p - g_n) \frac{\langle \boldsymbol{j}^2_R \rangle}{\langle \boldsymbol{I}^2 \rangle} \Bigg]. \end{aligned} \tag{13}$$

This enables a more refined examination of the g-factor phenomenon and facilitates a deeper exploration of the underlying physical mechanisms at play.

For the total spin state $|IM\rangle$ derived from a single coupling scheme within the weak-coupling basis (4), it is possible to analytically calculate its g factor by employing angular momentum algebra. The matrix elements of the squares and scalar products appearing in Eq. (10) for this particular single coupling scheme can be expressed as follows [43]:

$$\langle (j'_p j'_n) j'_{pn} j'_R; IM | \boldsymbol{j}^2_p | (j_p j_n) j_{pn} j_R; IM \rangle = \delta_{j'_p j_p} \delta_{j'_n j_n} \delta_{j'_R j_R} \delta_{j'_{pn} j_{pn}} j_p(j_p+1), \tag{14}$$

$$\langle (j'_p j'_n) j'_{pn} j'_R; IM | \boldsymbol{j}^2_n | (j_p j_n) j_{pn} j_R; IM \rangle = \delta_{j'_p j_p} \delta_{j'_n j_n} \delta_{j'_R j_R} \delta_{j'_{pn} j_{pn}} j_n(j_n+1), \tag{15}$$

$$\langle (j'_p j'_n) j'_{pn} j'_R; IM | \boldsymbol{j}^2_R | (j_p j_n) j_{pn} j_R; IM \rangle = \delta_{j'_p j_p} \delta_{j'_n j_n} \delta_{j'_R j_R} \delta_{j'_{pn} j_{pn}} j_R(j_R+1), \tag{16}$$

$$\begin{aligned} \langle (j'_p j'_n) j'_{pn} j'_R; IM | \boldsymbol{j}_p \cdot \boldsymbol{j}_n | (j_p j_n) j_{pn} j_R; IM \rangle &= \delta_{j'_p j_p} \delta_{j'_n j_n} \delta_{j'_R j_R} \delta_{j'_{pn} j_{pn}} (-1)^{j_p + j_n + j_{pn}} \\ &\times \sqrt{j_p(j_p+1)(2j_p+1)} \sqrt{j_n(j_n+1)(2j_n+1)} \begin{Bmatrix} j_p & j_n & j_{pn} \\ j_n & j_p & 1 \end{Bmatrix}, \end{aligned} \tag{17}$$

$$\begin{aligned} \langle (j'_p j'_n) j'_{pn} j'_R; IM | \boldsymbol{j}_p \cdot \boldsymbol{j}_R | (j_p j_n) j_{pn} j_R; IM \rangle &= \delta_{j'_p j_p} \delta_{j'_n j_n} \delta_{j'_R j_R} (-1)^{j_R + j_p + j_n + I + 1} \sqrt{(2j_{pn}+1)(2j'_{pn}+1)} \sqrt{j_p(j_p+1)(2j_p+1)} \\ &\times \sqrt{j_R(j_R+1)(2j_R+1)} \begin{Bmatrix} j_p & j_{pn} & j_n \\ j'_{pn} & j_p & 1 \end{Bmatrix} \begin{Bmatrix} j_{pn} & j_R & I \\ j_R & j'_{pn} & 1 \end{Bmatrix}, \end{aligned} \tag{18}$$

$$\langle (j'_p j'_n) j'_{pn} j'_R; IM | \boldsymbol{j}_n \cdot \boldsymbol{j}_R | (j_p j_n) j_{pn} j_R; IM \rangle = \delta_{j'_p j_p} \delta_{j'_n j_n} \delta_{j'_R j_R} (-1)^{j_R + j_p + j_n + I + 1 + j_{pn} + j'_{pn}} \sqrt{(2j_{pn}+1)(2j'_{pn}+1)} \sqrt{j_n(j_n+1)(2j_n+1)} \times \sqrt{j_R(j_R+1)(2j_R+1)} \begin{Bmatrix} j_n & j_{pn} & j_p \\ j'_{pn} & j_n & 1 \end{Bmatrix} \begin{Bmatrix} j_{pn} & j_R & I \\ j_R & j'_{pn} & 1 \end{Bmatrix}, \quad (19)$$

where nonzero values of the six-j symbols give all possible coupling schemes. These analytical expressions enable the determination of the g factor for the given single coupling scheme, allowing for a precise quantitative evaluation of the magnetic properties associated with the total spin state $|IM\rangle$. One can calculate the set of the g-factor values corresponding to possible coupling schemes by substituting the matrix elements (14)–(19) together with the values of g_p, g_n, and g_R into Eq. (10).

It is important to note that the matrix elements (14)–(19) are valid only when $j'_R = j_R$. This condition implies that the g factor can be decomposed into a summation of contributions from different j_R values. In other words, the g factor can be expressed as

$$g(I) = \sum_{j_R} g(j_R). \quad (20)$$

This decomposition allows for a detailed analysis and understanding of the individual contributions of different j_R values to the overall g factor. By considering these contributions separately, one can gain insights into the specific effects and influences of each j_R value on the magnetic properties of the system. Therefore, this decomposition offers a valuable approach to examine and interpret the underlying physics governing the g factor within the given context.

III. NUMERICAL DETAILS

In the calculations, I consider a system consisting of one proton particle in the $h_{11/2}$ state and one neutron hole in the $h_{11/2}$ state. This system is coupled to a triaxial rigid rotor with quadrupole deformation parameters $\beta = 0.23$ and a triaxial deformation parameter γ ranging from 0° to 60°. In this configuration, the 1 axis, the 2 axis, and the 3 axis correspond to the intermediate (m), short (s), and long (l) axes of the ellipsoid, respectively. To account for the rotational motion, moments of inertia of the irrotational flow type are employed, given by $\mathcal{J}_k = \mathcal{J}_0 \sin^2(\gamma - 2k\pi/3)$ ($k = 1$, 2, and 3), with $\mathcal{J}_0 = 30\hbar^2/\text{MeV}$. For the calculation of the g factor, I have utilized the adopted values of $g_p = 1.21$ for the proton, $g_n = -0.21$ for the neutron, and $g_R = 0.41$ for the core. These specific g-factor values have been incorporated to account for the individual components of the system.

IV. RESULTS AND DISCUSSIONS

For the particle-hole configuration under consideration, namely, $\pi(1h_{11/2})^1 \otimes \nu(1h_{11/2})^{-1}$, and within the range of $15^\circ \leqslant \gamma \leqslant 45^\circ$, previous investigations documented in Refs. [1,31,36–39,54,55] have established the presence of what is commonly referred to as chiral geometry within a specific range of spin values. These earlier investigations have extensively explored various aspects of this system, including the energy spectra, electromagnetic transition probabilities, static quadrupole moments, and the overall angular momentum geometry. Detailed results pertaining to these quantities can be found in the aforementioned references. In the present work, my primary focus lies in studying the behavior of the g factor for this particular system. I aim to contribute to the understanding of the g-factor behavior associated with the observed chiral geometry within the specified range of γ values.

A. Influences of deformation and moment of inertia

I first study the influences of deformation and moment of inertia on the g factor. In Fig. 1, I present the computed g factors for the yrast and yrare states of the $\pi(1h_{11/2})^1 \otimes \nu(1h_{11/2})^{-1}$ configuration at $I = 9\hbar$ within the PRM. The g factors are examined as a function of (a) the moment of inertia $\mathcal{J}_0$, while keeping deformation parameters $\beta = 0.23$ and $\gamma = 30^\circ$ constant; (b) the deformation parameter β, with $\mathcal{J}_0$ fixed at $30\,\hbar^2/\text{MeV}$ and $\gamma = 30^\circ$; and (c) the triaxial deformation parameter γ, with $\mathcal{J}_0$ maintained at $30\,\hbar^2/\text{MeV}$ and $\beta = 0.23$.

From the analysis, it becomes evident that the g factor shows limited sensitivity to both the moment of inertia $\mathcal{J}_0$ and the deformation parameter β. In contrast, the g factor exhibits notable dependence on the value of the triaxial deformation parameter γ. I have further checked that the similar sensitivity with respect to γ can be observed for the higher and lower β values compared to the chosen value of $\beta = 0.23$, as illustrated in Fig. 1(c) for $\beta = 0.10$ and 0.35. Moreover, the g factor demonstrates symmetry about the point $\gamma = 30^\circ$. Within the near prolate region ($\gamma \leqslant 10^\circ$) and the near oblate region ($\gamma \geqslant 50^\circ$), the g factor remains relatively constant. Outside these two regions, distinct trends can be observed for the yrast and yrare states as γ increases. Specifically, the

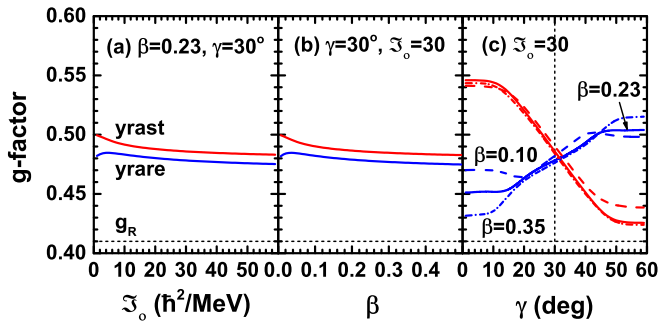

FIG. 1. The g factors for the yrast and yrare states associated with the particle-hole configuration $\pi(1h_{11/2})^1 \otimes \nu(1h_{11/2})^{-1}$ configuration calculated within the PRM at $I = 9\hbar$ as functions of (a) the moment of inertia $\mathcal{J}_0$, (b) the quadrupole deformation parameter β, and (c) the triaxial deformation parameter γ. The dotted lines represent the g factor for the rotor $g_R = 0.41$.

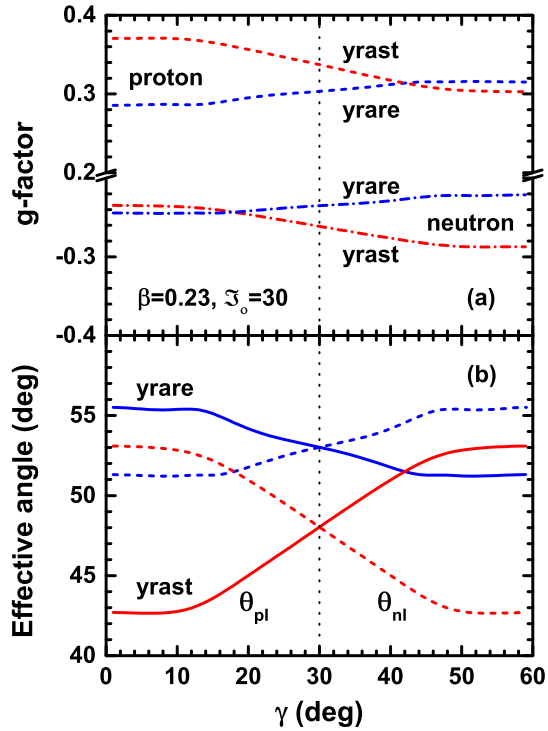

FIG. 2. (a) Contributions from the valence proton particle $g^{(p)}$ and neutron hole $g^{(n)}$ to the g factors of both the yrast and yrare states as a function of γ with with a fixed deformation parameter of $\beta = 0.23$ and a constant moment of inertia of $\mathcal{J}_0 = 30\,\hbar^2/\text{MeV}$, at $I = 9\hbar$. (b) The corresponding effective angles θ_{pI} and θ_{nI} of yrast and yrare bands.

g factor of the yrast state decreases, while that of the yrare state increases. This contrasting behavior between the doublet states highlights the impact of varying triaxial deformation on their respective g factors. This analysis provides valuable insights into the relationship between nuclear structure and the observed trends in the g factors for these specific particle-hole configurations.

In order to gain a deeper understanding of the behavior of the g factors with respect to the triaxial deformation parameter γ, I analyze the contributions from the valence proton particle $g^{(p)}$ (11) and neutron hole $g^{(n)}$ (12) to the g factors of both the yrast and yrare states. This analysis is conducted under specific conditions, with a fixed deformation parameter of $\beta = 0.23$ and a constant moment of inertia of $\mathcal{J}_0 = 30\,\hbar^2/\text{MeV}$, at an angular momentum value of $I = 9\hbar$. The contributions $g^{(p)}$ and $g^{(n)}$ are presented in Fig. 2. To illustrate these contributions, I present in Fig. 2 the corresponding effective angles denoted as θ_{pI} and θ_{nI} for the yrast and yrare states, respectively.

Upon analyzing the contributions of the valence proton $g^{(p)}$ and neutron $g^{(n)}$ to the g factors of the yrast and yrare bands, one observes distinct trends. Specifically, for the yrast state, both $g^{(p)}$ and $g^{(n)}$ decrease as the triaxial deformation parameter γ increases. In contrast, for the yrare state, both $g^{(p)}$ and $g^{(n)}$ exhibit an increase with increasing γ. These observed trends can be attributed to two primary factors. First, the angle θ_{pI} (θ_{nI}), which represents the effective angle associated with the valence proton particle (neutron hole) configuration, shows a contrasting behavior between the yrast and yrare states. Specifically, in the yrast state, θ_{pI} increases with increasing γ, while in the yrare state, it decreases with increasing γ. Second, the signs of the differences $g_p - g_R = 0.80$ and $g_n - g_R = -0.62$ appearing in the g-factor formula Eq. (10) are opposite. These differences determine the contribution of the valence proton and neutron to the total g factors. The contrasting signs of these differences further contribute to the different trends observed in the yrast and yrare bands as γ increases.

At this stage, one can understand that the distinct sensitivities of the g factor to the β and γ deformation parameters stem from two underlying physical aspects. First, the irrotational flow type moments of inertia $\mathcal{J}_k = \mathcal{J}_0 \sin^2(\gamma - 2k\pi/3)$ employed in my model, and the resulting ratios between the three principal axis moments of inertia, are sensitive to the γ deformation parameter while remaining independent of β. Second, the γ dependence in the single-j shell Hamiltonian (3) used in the model governs the angular momentum properties of the proton particle and the neutron hole. Specifically, the angular momentum component of the proton particle along the s axis is equal to that along the m axis at $\gamma \approx 0^\circ$. However, when $\gamma \approx 30^\circ$, the angular momentum component along the s axis becomes significantly larger than that along the m axis. Both of these physical factors have a direct and consequential impact on the effective angles θ_{pI} and θ_{nI}, which ultimately influence the values of the g factor.

B. Influences of total spin

The combination of the valence proton particle angular momentum $\boldsymbol{j}_p$, the valence neutron hole angular momentum $\boldsymbol{j}_n$, and the core angular momentum $\boldsymbol{j}_R$ results in the formation of the total spin $\boldsymbol{I}$ for the studied system. It has been extensively established in the literature, as documented in Refs. [37,38,42,56,57], that the presence of chiral rotations, which refer to nonplanar rotations of the total angular momentum, manifests only above a critical spin value I. At lower spins, a different phenomenon known as chiral vibration occurs, characterized by an oscillation of the total angular momentum between left- and right-handed configurations. Conversely, at higher spins, a chiral rotation takes place.

To investigate the influence of collective rotation on the g factor, I have examined the g factors of the yrast and yrare bands in the $\pi(1h_{11/2})^1 \otimes \nu(1h_{11/2})^{-1}$ configuration as functions of spin, considering various triaxial deformation parameters ($\gamma = 0^\circ, 10^\circ, 20^\circ, 30^\circ, 40^\circ, 50^\circ$, and 60°). Figure 3 depicts these variations, including the cases when the valence proton and neutron angular momenta are parallel to the total angular momentum ($\boldsymbol{j}_p \parallel \boldsymbol{j}_n \parallel \boldsymbol{I}$), perpendicular to each other and to the rotor angular momentum $\boldsymbol{j}_p \perp \boldsymbol{j}_n \perp \boldsymbol{j}_R$ [i.e., g_{chiral} in Eq. (13)], as well as the g factor of the rotor g_R. In addition, to illustrate the changes in these configurations, Fig. 4 presents the effective angles θ_{pI} and θ_{nI} for the yrast and yrare bands in the $\pi(1h_{11/2})^1 \otimes \nu(1h_{11/2})^{-1}$ configuration as functions of spin, considering $\gamma = 0^\circ, 10^\circ, 20^\circ$, and 30°.

For the case of $\gamma = 30^\circ$, previous work in Ref. [37] has provided a comprehensive understanding of the evolution of

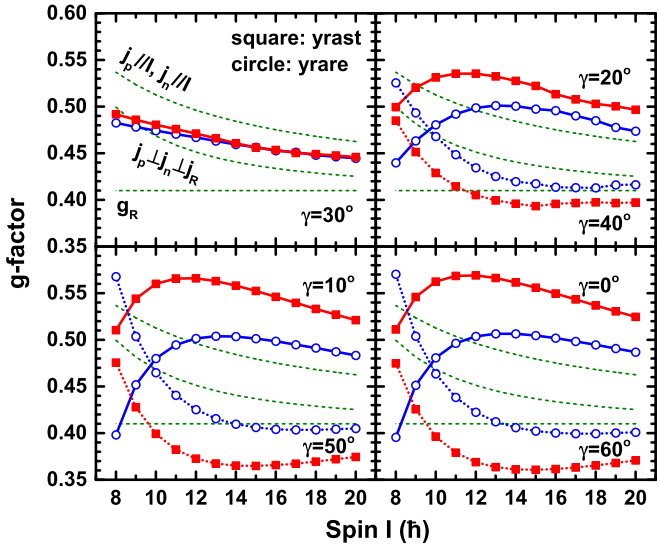

FIG. 3. The g factors of the yrast and yrare bands for the $\pi(1h_{11/2})^1 \otimes \nu(1h_{11/2})^{-1}$ configuration as functions of spin at $\gamma = 0°$, $10°$, $20°$, $30°$, $40°$, $50°$, and $60°$. The dashed lines represent the cases when $\boldsymbol{j}_p \parallel \boldsymbol{j}_n \parallel \boldsymbol{I}$, $\boldsymbol{j}_p \perp \boldsymbol{j}_n \perp \boldsymbol{j}_R$, and the g factor of the rotor g_R.

the chiral mode in this system. The analysis was conducted using an azimuthal plot of the total angular momentum, revealing a transition from planar to aplanar rotation as the rotational mode of the system changes. It was found that this transition occurs at a critical spin value of $I = 13\hbar$. In accordance with this rotational transition, the g factors of the yrast and yrare bands were observed to decrease with increasing spin I, as illustrated in Fig. 3. Notably, these g factors exhibit striking similarities, especially within the region of static chirality ($I \geqslant 13\hbar$) described in Refs. [37,38]. In fact, they become nearly identical within this regime.

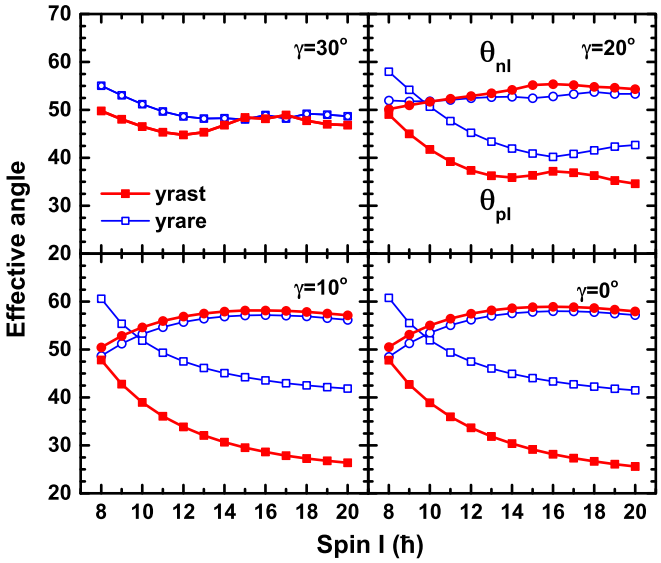

FIG. 4. The effective angles θ_{pI} and θ_{nI} (in degrees) of the yrast and yrare bands for the $\pi(1h_{11/2})^1 \otimes \nu(1h_{11/2})^{-1}$ configuration as functions of spin at $\gamma = 0°$, $10°$, $20°$, and $30°$.

Moreover, the corresponding effective angles θ_{pI} and θ_{nI} of the doublet bands, as depicted in Fig. 4, demonstrate that they are quite similar for spins $I \leqslant 13\hbar$ and converge as I exceeds $14\hbar$. Therefore, the similarity in g factors can be regarded as a distinctive characteristic of static chirality. Furthermore, it is worth noting that the g factors calculated using the PRM closely resemble those obtained in the limit of $g_{\rm chiral}$ ($\boldsymbol{j}_p \perp \boldsymbol{j}_n \perp \boldsymbol{j}_R$) near the bandhead. However, it is important to clarify that this does not necessarily indicate the presence of chiral rotation at the bandhead. Instead, this similarity arises due to the fact that the angular momentum of the rotor is significantly smaller than that of the proton and neutron in the vicinity of the bandhead, as elucidated in Ref. [37]. Within the region of static chirality, the g factors calculated by the PRM deviate from the $g_{\rm chiral}$ ($\boldsymbol{j}_p \perp \boldsymbol{j}_n \perp \boldsymbol{j}_R$) limit, suggesting that the ideal aplanar rotation is not fully realized in the PRM calculations. It is important to note that the total Hamiltonian for the present symmetric particle-hole configuration with an irrotational flow type of moment of inertia is invariant under the transformation $\gamma \to 60° - \gamma$. Consequently, the g factors obtained using γ and $60° - \gamma$ exhibit symmetry with respect to those obtained using $\gamma = 30°$, as exhibited in Fig. 3. This symmetry is reflected in the increasing-decreasing behavior of the g factors of the doublet bands for $\gamma < 30°$ and the decreasing-increasing trend observed for $\gamma > 30°$. However, one can observe that the g factors of the doublet bands are not similar to those observed at $\gamma = 30°$. Specifically, for $\gamma < 30°$, the g factors of the yrast band are larger than those of the yrare band for a given spin, while the opposite trend is observed for $\gamma > 30°$. Additionally, the differences between the g factors of the doublet bands decrease with increasing spin. A previous study [38] demonstrated that chiral geometry does not occur at $\gamma = 10°$ and $0°$, where the energy difference between the doublet bands is considerably large. In these cases, the angular momentum exhibits planar rotation modes, i.e., lacking the chirality. The large difference in g factors between the doublet bands observed at $\gamma = 10°$ and $0°$ confirms this conclusion.

The behaviors of the g factors can be comprehended by examining the plots of the effective angles θ_{pI} and θ_{nI} at $\gamma = 20°$, $10°$, and $0°$, as illustrated in Fig. 4. It is observed that the θ_{nI} values for the doublet bands exhibit similar slight increasing trends. However, the θ_{pI} values for the doublet bands differ significantly. Specifically, the θ_{pI} value for the yrare band is greater than that of the yrast band. The magnitude of this difference becomes more pronounced as γ deviates from $\gamma = 30°$, resulting in the larger differences between the g factors of the doublet bands (cf. Fig. 3). Furthermore, the θ_{pI} values demonstrate a decreasing trend, suggesting that the proton angular momentum approaches the total angular momentum as the spin increases. Consequently, the g factors of the doublet bands exhibit an increasing behavior, as depicted in Fig. 3.

C. Influences of rotor angular momentum

As previously mentioned, the g factor can be expressed as a sum of contributions from various j_R values. In Fig. 5, I present the g factor components $g(j_R)$ as a function of R for

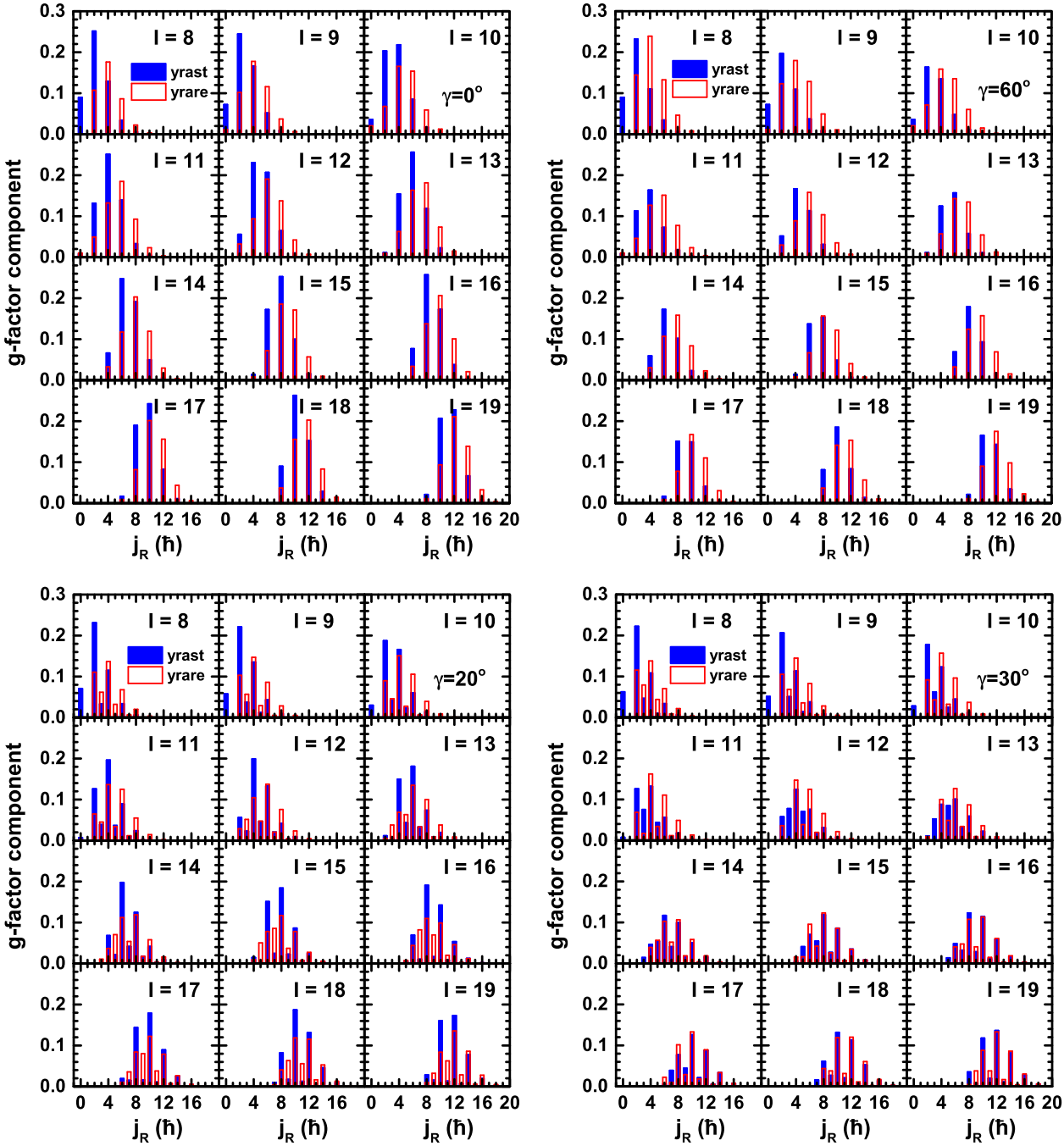

FIG. 5. Contributions to the g factors of the yrast and yrare bands as functions of rotor angular momentum j_R at triaxial deformation parameters $\gamma = 0°$, $20°$, $30°$, and $60°$.

the yrast and yrare bands calculated at $\gamma = 0°$, $20°$, $30°$, and $60°$. An examination of the figure reveals that as the total spin I increases, the distributions of $g(j_R)$ progressively shift their weights from the low-R region to the high-R region, indicating a gradual rise in the rotor angular momentum.

At $\gamma = 0°$ and $60°$, the quantum number R can only take even integer values, as its three-axis component in the intrinsic frame K_R must be zero. Consequently, the distribution $g(j_R)$ is zero for odd R. When looking at the $g(j_R)$ plots for the yrast and yrare bands across the entire spin range of $8\hbar \leqslant I \leqslant 20\hbar$, they exhibit distinct behaviors. The weights assigned to each R value, as well as the positions of the maxima, differ between the two bands. Specifically, in the yrare band, the R value associated with the maximum weight is consistently $2\hbar$ larger than that in the yrast band. This behavior aligns with the significant energy difference [38] and significant g-factor difference (cf. Fig. 3) observed between the doublet bands.

At $\gamma = 20°$, the contributions from odd R values become more significant. This can be attributed to the decreasing energies of the rotor associated with odd R, which gradually become comparable to those of even R at $\gamma = 20°$ [38,58]. For $I \leqslant 12\hbar$, the R value corresponding to the maximum $g(j_R)$ in

the yrare band remains consistently $2\hbar$ larger than that in the yrast band. However, for $I \geqslant 13\hbar$, the $g(j_R)$ plots for the yrast and yrare bands exhibit similar patterns, although noticeable differences in the detailed amplitudes persist. This similarity aligns with the small energy differences (less than 300 keV) [38] and closer g factor (cf. Fig. 3) observed between the doublet bands in this spin region.

At $\gamma = 30^\circ$, the most notable characteristic is the striking similarity between the $g(j_R)$ plots of the yrast and yrare bands for $I \geqslant 14\hbar$, both in terms of the distribution patterns and the amplitudes. These properties are consistent with the nearly degenerate nature of the doublet bands observed in this scenario [38]. Consequently, the g factors of the doublet bands exhibit a high degree of similarity, as illustrated in Fig. 3.

V. SUMMARY

In summary, extensive investigations have been conducted to explore the g factor of chiral doublet bands using the particle rotor model. The focus of these studies has been on systems characterized by the particle-hole configuration $\pi(1h_{11/2})^1 \otimes \nu(1h_{11/2})^{-1}$. A comprehensive examination has been carried out to evaluate the influence of deformation parameters β and γ, the moment of inertia $\mathcal{J}_0$, the total spin I, and the angular momentum of the collective rotor j_R on the g factor.

The key conclusions derived from these investigations can be summarized as follows.

(i) The variation in the γ parameter significantly affects the behavior of the g factor, emphasizing its sensitivity to this particular parameter.

(ii) The g factor demonstrates little sensitivity to changes in the deformation parameter β and the moment of inertia $\mathcal{J}_0$.

(iii) The total spin I and the angular momentum of the collective rotor j_R play significant roles in affecting the g factor.

(iv) The g factors and corresponding $g(j_R)$ plots for the doublet bands exhibit significant similarities in the region of static chirality, while differences become apparent in regions characterized by chiral vibration or the absence of chirality.

These findings provide valuable insights into the complex behavior and underlying physics of chiral doublet bands.

Presently, experimental measurements of the g factor in relation to chiral rotation have primarily been conducted solely for the bandhead of ^{128}Cs [42,43]. This limited scope accentuates the need for future experimental endeavors to concentrate on quantifying the g factor for a broader range of chiral doublet bands. By conducting such measurements, a more comprehensive understanding of the behavior of chiral doublet bands can be obtained. The systematic characterization of the g factor across a wider spectrum of chiral doublet bands will provide crucial insights into the underlying physics that governs these systems. Consequently, it is strongly advocated that future investigations prioritize the measurement of the g factor for various chiral doublet bands to advance the understanding of their magnetic behavior.

ACKNOWLEDGMENTS

I thank E. Grodner, J. Meng, J. Srebrny, S. Q. Zhang, and P. W. Zhao for helpful discussions. This work was supported by the National Natural Science Foundation of China under Grant No. 12205103.

[1] S. Frauendorf and J. Meng, Nucl. Phys. A **617**, 131 (1997).
[2] J. Meng and S. Q. Zhang, J. Phys. G: Nucl. Part. Phys. **37**, 064025 (2010).
[3] J. Meng, Q. B. Chen, and S. Q. Zhang, Int. J. Mod. Phys. E **23**, 1430016 (2014).
[4] R. A. Bark, E. O. Lieder, R. M. Lieder, E. A. Lawrie, J. J. Lawrie, S. P. Bvumbi, N. Y. Kheswa, S. S. Ntshangase, T. E. Madiba, P. L. Masiteng *et al.*, Int. J. Mod. Phys. E **23**, 1461001 (2014).
[5] J. Meng and P. W. Zhao, Phys. Scr. **91**, 053008 (2016).
[6] A. A. Raduta, Prog. Part. Nucl. Phys. **90**, 241 (2016).
[7] K. Starosta and T. Koike, Phys. Scr. **92**, 093002 (2017).
[8] S. Frauendorf, Phys. Scr. **93**, 043003 (2018).
[9] Q. B. Chen and J. Meng, Nucl. Phys. News **30**, 11 (2020).
[10] B. W. Xiong and Y. Y. Wang, At. Data Nucl. Data Tables **125**, 193 (2019).
[11] J. Meng, J. Peng, S. Q. Zhang, and S.-G. Zhou, Phys. Rev. C **73**, 037303 (2006).
[12] J. Peng, H. Sagawa, S. Q. Zhang, J. M. Yao, Y. Zhang, and J. Meng, Phys. Rev. C **77**, 024309 (2008).
[13] J. M. Yao, B. Qi, S. Q. Zhang, J. Peng, S. Y. Wang, and J. Meng, Phys. Rev. C **79**, 067302 (2009).
[14] J. Li, S. Q. Zhang, and J. Meng, Phys. Rev. C **83**, 037301 (2011).
[15] J. Peng and Q. B. Chen, Phys. Rev. C **98**, 024320 (2018).
[16] B. Qi, H. Jia, C. Liu, and S. Y. Wang, Phys. Rev. C **98**, 014305 (2018).
[17] J. Li, Phys. Rev. C **97**, 034306 (2018).
[18] A. D. Ayangeakaa, U. Garg, M. D. Anthony, S. Frauendorf, J. T. Matta, B. K. Nayak, D. Patel, Q. B. Chen, S. Q. Zhang, P. W. Zhao *et al.*, Phys. Rev. Lett. **110**, 172504 (2013).
[19] I. Kuti, Q. B. Chen, J. Timár, D. Sohler, S. Q. Zhang, Z. H. Zhang, P. W. Zhao, J. Meng, K. Starosta, T. Koike *et al.*, Phys. Rev. Lett. **113**, 032501 (2014).
[20] C. Liu, S. Y. Wang, R. A. Bark, S. Q. Zhang, J. Meng, B. Qi, P. Jones, S. M. Wyngaardt, J. Zhao, C. Xu *et al.*, Phys. Rev. Lett. **116**, 112501 (2016).
[21] C. M. Petrache, B. F. Lv, A. Astier, E. Dupont, Y. K. Wang, S. Q. Zhang, P. W. Zhao, Z. X. Ren, J. Meng, P. T. Greenlees *et al.*, Phys. Rev. C **97**, 041304(R) (2018).
[22] T. Roy, G. Mukherjee, M. Asgar, S. Bhattacharyya, S. Bhattacharya, C. Bhattacharya, S. Bhattacharya, T. Ghosh, K. Banerjee, S. Kundu *et al.*, Phys. Lett. B **782**, 768 (2018).

[23] B. F. Lv, C. M. Petrache, Q. B. Chen, J. Meng, A. Astier, E. Dupont, P. Greenlees, H. Badran, T. Calverley, D. M. Cox *et al.*, Phys. Rev. C **100**, 024314 (2019).

[24] C. M. Petrache, B. F. Lv, Q. B. Chen, J. Meng, A. Astier, E. Dupont, K. K. Zheng, P. T. Greenlees, H. Badran, T. Calverley *et al.*, Eur. Phys. J. A **56**, 208 (2020).

[25] S. Guo, C. M. Petrache, D. Mengoni, Y. H. Qiang, Y. P. Wang, Y. Y. Wang, J. Meng, Y. K. Wang, S. Q. Zhang, P. W. Zhao *et al.*, Phys. Lett. B **807**, 135572 (2020).

[26] L. Mu, S. Y. Wang, C. Liu, B. Qi, R. A. Bark, J. Meng, S. Q. Zhang, P. Jones, S. M. Wyngaardt, H. Jia *et al.*, Phys. Lett. B **827**, 137006 (2022).

[27] T. Koike, K. Starosta, and I. Hamamoto, Phys. Rev. Lett. **93**, 172502 (2004).

[28] E. Grodner, J. Srebrny, A. A. Pasternak, I. Zalewska, T. Morek, C. Droste, J. Mierzejewski, M. Kowalczyk, J. Kownacki, M. Kisielinski *et al.*, Phys. Rev. Lett. **97**, 172501 (2006).

[29] D. Tonev, G. de Angelis, P. Petkov, A. Dewald, S. Brant, S. Frauendorf, D. L. Balabanski, P. Pejovic, D. Bazzacco, P. Bednarczyk *et al.*, Phys. Rev. Lett. **96**, 052501 (2006).

[30] S. Mukhopadhyay, D. Almehed, U. Garg, S. Frauendorf, T. Li, P. V. Madhusudhana Rao, X. Wang, S. S. Ghugre, M. P. Carpenter, S. Gros, A. Hecht, R. V. F. Janssens, F. G. Kondev, T. Lauritsen, D. Seweryniak, and S. Zhu, Phys. Rev. Lett. **99**, 172501 (2007).

[31] B. Qi, S. Q. Zhang, S. Y. Wang, J. M. Yao, and J. Meng, Phys. Rev. C **79**, 041302(R) (2009).

[32] E. Grodner, I. Sankowska, T. Morek, S. G. Rohozinski, C. Droste, J. Srebrny, A. A. Pasternak, M. Kisielinski, M. Kowalczyk, J. Kownacki *et al.*, Phys. Lett. B **703**, 46 (2011).

[33] D. Tonev, M. S. Yavahchova, N. Goutev, G. de Angelis, P. Petkov, R. K. Bhowmik, R. P. Singh, S. Muralithar, N. Madhavan, R. Kumar *et al.*, Phys. Rev. Lett. **112**, 052501 (2014).

[34] E. O. Lieder, R. M. Lieder, R. A. Bark, Q. B. Chen, S. Q. Zhang, J. Meng, E. A. Lawrie, J. J. Lawrie, S. P. Bvumbi, N. Y. Kheswa *et al.*, Phys. Rev. Lett. **112**, 202502 (2014).

[35] N. Rather, P. Datta, S. Chattopadhyay, S. Rajbanshi, A. Goswami, G. H. Bhat, J. A. Sheikh, S. Roy, R. Palit, S. Pal *et al.*, Phys. Rev. Lett. **112**, 202503 (2014).

[36] Q. B. Chen, K. Starosta, and T. Koike, Phys. Rev. C **97**, 041303(R) (2018).

[37] Q. B. Chen and J. Meng, Phys. Rev. C **98**, 031303(R) (2018).

[38] Q. B. Chen, N. Kaiser, U.-G. Meißner, and J. Meng, Phys. Rev. C **99**, 064326 (2019).

[39] Q. B. Chen, N. Kaiser, U.-G. Meißner, and J. Meng, Phys. Lett. B **807**, 135568 (2020).

[40] Q. B. Chen, S. Frauendorf, N. Kaiser, U.-G. Meißner, and J. Meng, Phys. Lett. B **807**, 135596 (2020).

[41] C. Broocks, Q. B. Chen, N. Kaiser, and U.-G. Meißner, Eur. Phys. J. A **57**, 161 (2021).

[42] E. Grodner, J. Srebrny, C. Droste, L. Próchniak, S. G. Rohoziński, M. Kowalczyk, M. Ionescu-Bujor, C. A. Ur, K. Starosta, T. Ahn *et al.*, Phys. Rev. Lett. **120**, 022502 (2018).

[43] E. Grodner, M. Kowalczyk, M. Kisieliski, J. Srebrny, L. Próchniak, C. Droste, S. G. Rohoziński, Q. B. Chen, M. Ionescu-Bujor, C. A. Ur, F. Recchia, J. Meng, S. Q. Zhang, P. W. Zhao, G. Georgiev, R. Lozeva, E. Fiori, S. Aydin, and A. Nalecz-Jawecki, Phys. Rev. C **106**, 014318 (2022).

[44] J. Peng, J. Meng, and S. Q. Zhang, Phys. Rev. C **68**, 044324 (2003).

[45] S. Q. Zhang, B. Qi, S. Y. Wang, and J. Meng, Phys. Rev. C **75**, 044307 (2007).

[46] B. Qi, S. Q. Zhang, J. Meng, S. Y. Wang, and S. Frauendorf, Phys. Lett. B **675**, 175 (2009).

[47] E. A. Lawrie and O. Shirinda, Phys. Lett. B **689**, 66 (2010).

[48] Q. B. Chen, B. F. Lv, C. M. Petrache, and J. Meng, Phys. Lett. B **782**, 744 (2018).

[49] Y. Y. Wang, S. Q. Zhang, P. W. Zhao, and J. Meng, Phys. Lett. B **792**, 454 (2019).

[50] J. Meng, in *Relativistic Density Functional for Nuclear Structure*, International review of nuclear physics (World Scientific, Singapore, 2016), Vol. 10.

[51] C. M. Petrache, Q. B. Chen, S. Guo, A. D. Ayangeakaa, U. Garg, J. T. Matta, B. K. Nayak, D. Patel, J. Meng, M. P. Carpenter *et al.*, Phys. Rev. C **94**, 064309 (2016).

[52] J. Peng and Q. B. Chen, Phys. Lett. B **793**, 303 (2019).

[53] J. Peng and Q. B. Chen, Phys. Lett. B **806**, 135489 (2020).

[54] Q. B. Chen, J. M. Yao, S. Q. Zhang, and B. Qi, Phys. Rev. C **82**, 067302 (2010).

[55] H. Zhang and Q. B. Chen, Chin. Phys. C **40**, 024101 (2016).

[56] P. Olbratowski, J. Dobaczewski, J. Dudek, and W. Płóciennik, Phys. Rev. Lett. **93**, 052501 (2004).

[57] P. Olbratowski, J. Dobaczewski, and J. Dudek, Phys. Rev. C **73**, 054308 (2006).

[58] A. S. Davydov and G. F. Filippov, Nucl. Phys. **8**, 237 (1958).